Aeolian Research 20 (2016) 126–138

Contents lists available at ScienceDirect

Aeolian Research

journal homepage: www.elsevier.com/locate/aeolia

PTV measurement of the spanwise component of aeolian transport in steady state

Patrick O'Brien, Cheryl McKenna Neuman *

Department of Geography, Trent University, Peterborough, ON K9J 7B8, Canada

ARTICLE INFO

Article history:
Received 17 June 2015
Revised 1 October 2015
Accepted 5 November 2015
Available online 11 January 2016

Keywords:
Particle Tracking Velocimetry
Aeolian transport
Wind tunnel Simulation

ABSTRACT

This paper outlines and validates an improved particle tracking technique (PTV-EPAS) with automated trajectory detection capabilities, and then reports on a novel set of wind tunnel experiments aimed at measuring all three velocity components simultaneously. In order to study a fully adjusted particle cloud, the entire floor of the tunnel was filled with quartz sand (median diameter 550 μm) and the freestream velocity set to 8 ms^{-1} at an elevation of 0.35 m, above the threshold for particle entrainment at 6.5 ms^{-1}. This produced a friction velocity (u^*) of ~0.38 ms^{-1} with u^*/u_t^* = 1.3. Measurement of particle trajectories aligned at a spanwise angle (θ) relative to the mean airflow along the center-line of the wind tunnel involved incrementally adjusting the light sheet orientation from 0° to 60°. Three replicate experiments were carried out for each of 13 angles. Only 12% of all 2×10^5 trajectories sampled were strictly aligned with the mean streamwise air flow, while 95% were contained within 45°. As θ increases, a greater proportion of the particle transport consists of slow moving ejecta that ascend from and then impact the bed surface at higher angles than observed for saltation.

1. Introduction

Geomorphologists have long recognized that sand transport by wind is fundamentally three-dimensional (3D) in nature. From micro-scale ripples and flutes etched into ventifact surfaces to large-scale dunes, evidence of this three-dimensionality is preserved in aeolian bedforms that are ubiquitous in dryland regions of the world. Over the last decade or more, considerable effort has been invested in studying the spatial components of the transport process, as for example, in CFD simulation of the airflow structures surrounding such bedforms (e.g. Jackson et al., 2011), and in observation of the horizontal instability of sand streamers associated with vortical structures present in the shearing flow near the bed surface (e.g. Baas and Sherman, 2005).

At the particle scale, however, the perspective remains primarily two-dimensional (2D). While some progress has been made very recently in extending numerical models to a 3D framework (e.g. Yang et al., 2010), no direct measurements have as yet captured simultaneously all three components (*x*-streamwise, *y*-spanwise, *z*-vertical) of the motion of individual sand grains. For the purposes of the present paper, saltation is recognized as the motion of particles in a succession of ballistic jumps that are governed by gravity and fluid drag. Saltators rise sufficiently high into the airflow to attain a forward acceleration by the wind, and upon impact with the surface, may splash other particles (reptators) out of the bed. High speed photography suggests that any given particle may engage in a continuum of transport modes before finally coming to rest on the bed surface (e.g. roll-hop-slide-roll etc.). In general, the existing techniques for observing the flight of discrete sand particles have been restricted to situations involving unrealistically low particle concentrations, as for example, constrained by either low wind speeds near the threshold for entrainment or particle supply limitation imposed by a short fetch length.

The current paper presents an improved particle tracking (PTV) technique; validates it using direct two-dimensional velocity measurements obtained with a Laser Doppler anemometer (LDA); and then, presents a novel investigation of all three particle velocity components (u_x, u_z, u_y) measured simultaneously in wind tunnel experiments wherein the boundary-layer was fully saturated with saltating sand grains. We begin, however, with providing a brief context for this work which reviews the existing technologies and selected measurements of saltation dynamics in 2D.

2. Literature review

2.1. Technologies for the measurement of particle motion

With regard to capturing data on particle motion within a saltation cloud, there are three principal technologies available: Laser

* Corresponding author. Tel.: +1 705 748 1011; fax: +1 705 748 1205.
E-mail address: cmckneuman@trentu.ca (C. McKenna Neuman).

http://dx.doi.org/10.1016/j.aeolia.2015.11.005
1875-9637/

List of symbols

x	streamwise direction
y	spanwise direction
z	vertical direction (elevation)
r	particle image radius
d	particle diameter
ρ	particle density
m_j	particle mass associated with the jth trajectory
n_k	total number of particle trajectory segments sampled within the kth plane
n_j	total number of particle images (where $i = 1, 2, 3 \ldots n_j$) representing the jth trajectory
N	total number of trajectories sampled within the particle cloud; may be segregated into subpopulations of ascending versus descending particles
A	area, e.g. field of view within the light sheet
θ	spanwise angle of the laser light sheet within the xy plane, i.e. at 0° the light sheet is oriented parallel to the airflow
α	angle of the particle's trajectory relative to the bed surface, where α_2 is the impact angle, α_1 the ejection angle and α_{50} the median angle
k	θ slice counter
t	time
U	mean velocity for a given particle along its flight path; equivalent to the instantaneous velocity (U') when the particle is not accelerated
U_{50}	median velocity based on the 50th percentile for a distribution of U
U_h	horizontal velocity of given particle moving parallel to the light sheet
u	velocity component for a given particle, where subscripts x (streamwise), y (spanwise) and z (vertical) indicate the orientation of the vector according to the axis convention shown in Fig. 1
U_∞	Mean wind velocity within the freestream flow
u^*	friction velocity
u_t^*	threshold friction velocity
E	kinetic energy of a given particle (with directional components specified by subscripts x, y or z)
E_k	kinetic energy of all particles sampled within the kth spanwise plane
KE	total kinetic energy sampled over the full range of values for θ

Where specified, subscripts 1 and 2 refer to ascending and descending particles, respectively.

Doppler Anemometry (LDA), Particle Imaging Velocimetry (PIV), and Particle Tracking Velocimetry (PTV). LDA is useful for obtaining population statistics, but does not track individual particles and cannot be used at elevations (z) in close proximity to a sand bed (e.g. $z < 3$ mm) where its photosensor becomes overloaded. PIV can track individual sand particles, but only for sequential high speed images that are paired. The displacement distance measured is in the order of several particle diameters (or less) and generally represents an insignificant fraction of the ballistic trajectory. PIV is unable to perform reliably in flows where there is a high density of sand particles of various sizes.

PTV is widely regarded as the most desirable method for obtaining information about saltation dynamics as this technology can track a particle's displacement and velocity throughout a portion of its ballistic trajectory, in rare instances from ejection through to impact (or a complete 'life cycle'). The basis of this methodology involves a thin (~1.5 mm) laser light sheet aligned parallel to the wind direction (Fig. 1), within which saltating particles are illuminated as they pass through it. Their paths are recorded with a high speed camera oriented perpendicular to the sheet. The image of a given particle in one camera frame is then correlated with other images of the same particle across sequential frames to produce a record of the grain's trajectory during the entire sampling period. From this record, particle velocity, angle and acceleration/deceleration can be calculated during ascending and descending phases. The evolution of PTV has yielded numerous papers that examine selected aspects of saltation at a micro-scale in 2D, as for example, particle spin (White and Shulz, 1977), surface collision (Gordon and McKenna Neuman, 2009), and ejection and impact statistics (Zhang et al., 2014). Similar to LDA and PIV technologies, however, existing PTV systems generally perform poorly in airflows with a high density of particles, especially near the bed surface where the particle concentration is highest (Liu and Dong, 2004) and in saturated or transport limited conditions.

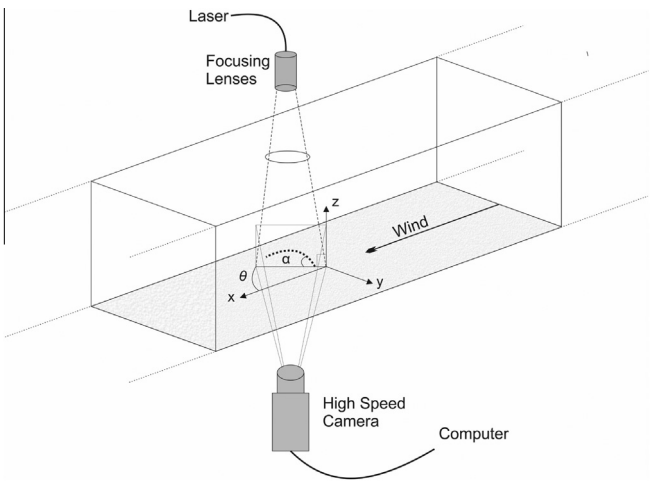

Fig. 1. Schematic of PTV system configuration, along with directional naming conventions.

The earliest PTV experiments were conducted using cine film photography with manual particle identification and tracking (Rice et al., 1995, 1996; White and Shulz, 1977). While the high speed of these film cameras (~3000 fps) was suitable for capturing the full range of particle velocities possible, they could only sample in relatively low saltation densities as typical of those generated by emissions from either a short tray or narrow strip of sand. Manual processing of the images was subjective, and due to its labor intensive nature, not feasible for processing large data sets. Over the last decade, scientific-grade, digital cameras have replaced film in the application of PTV in wind tunnel experiments (Zhang et al., 2007; Wang et al., 2008; Beladjine et al., 2007). The digital images captured by these cameras have the advantage that particles can be automatically detected and assigned spatial coordinates using a range of commercial and customized computer programs. However, the manual assignment of particle images to trajectories remains a constraint in the analysis of very large populations of saltators. A further disadvantage of early digital PTV technology was that cameras delivering both high resolution and a high frame rate were very costly. As a result, they were largely inaccessible to aeolian researchers, so that compromises were often made that affected the quality of the work. Within the last four years, a

number of wind tunnel studies of aeolian transport (e.g. Ho et al., 2014; Zhang et al., 2014; Gordon and McKenna Neuman, 2011) have employed state-of-the-art digital cameras to not only obtain good quality images at very high frame rates, but also detect both the sand particles and their trajectories automatically.

For reference, a select number of wind tunnel investigations of aeolian saltation involving PTV are evaluated in Table 1. The following list outlines the associated criteria (yes/no):

i. Digital camera.
ii. Automatic I: computer aided image processing to identify particles and assign spatial coordinates.
iii. Automatic II: trajectory identification and analysis.
iv. Frame rate (FPS): the camera is capable of capturing frames sufficiently fast that the entire distribution of particle velocities is sampled (>1000 feet per second, FPS).
v. Scale: cross sectional area of the wind tunnel is large enough that wall effects are relatively small and saltating particles do not bounce off the roof for the respective wind velocity (e.g. at least 0.5 m × 0.5 m or greater). The fetch of the tunnel working section is long enough for the concentration of particles within the saltation cloud to stabilize (e.g. 6 m or greater).
vi. Supply: bed of sand covers the entire floor area of the tunnel working section and is sufficiently long and deep to avoid constraint on the supply of particles from the surface to the airflow.
vii. Wind speed: wind speeds in the tunnel are varied in magnitude over a given range, and exceed that required for the entrainment of the bed material.
viii. Sampling range: PTV sampling is carried out over a two-dimensional plane extending from the surface of the test bed to the top of the saltation cloud.
ix. 3D: measurement of particle motion in three-dimensional space.

While PTV techniques have undoubtedly improved over the last decade, they are still primarily used in wind tunnel simulations of saltation that have significant limitations associated either with their experimental design or the scale of the facility. For a saltation cloud to reach an equilibrium or a saturated state, the boundary-layer flow within the wind tunnel must be fully adjusted to the mass transport in the absence of constraints associated with either the fetch length, wall effect, or particle supply. Table 1 shows that only a few aeolian transport studies using PTV have involved automated particle detection and trajectory identification, while such analyses have rarely been performed using images obtained within a fully saturated saltation cloud. There remain no PTV experiments that meet all of the identified criteria while obtaining information on particle saltation dynamics in three-dimensional space, inclusive of the cross-flow or span-wise component.

In Section 3, we describe improvements upon a PTV system developed by Gordon and McKenna Neuman (2009, 2011) that allow sampling at higher wind speeds and particle concentrations than previously possible. The system utilizes advanced camera technology and a new automatic tracking algorithm (EPAS) to observe particle trajectories over a wide range of velocities, and in a small number of instances from lift-off through to impact and rebound.

2.2. Saltation trajectory dynamics

A number of recent papers and book chapters provide comprehensive overviews of the physics of saltation, and specifically, the dynamics of particle trajectories within a two-dimensional framework (e.g. Creyseels et al., 2009; Shao, 2010; Kok et al., 2012; Duran et al., 2011; Valance et al., 2015), as obtained from measurements of saltation clouds produced within wind tunnel experiments and from physically-based, numerical simulations. It is beyond the scope of this paper to repeat this information, although a highly abbreviated overview is provided below in order to provide some context for the measurements obtained in this study. The reader is referred to the works cited for additional detail.

A saltating particle obtains momentum from the boundary-layer airflow, and in returning to the bed surface, strikes it with increased velocity. In a characteristic ballistic trajectory as assumed in early analytical models of uniform saltation (e.g. Bagnold, 1941; Owen, 1964), the impact angle (α_2) is typically taken to be ~13° as compared to that for lift-off (α_1) around ~55°. In reality, however, variations in the turbulent flow and in

Table 1
Summary and evaluation of wind tunnel experiments in which PTV has been employed to study sand transport. Column headings are explained in the main text. An asterisk (*) affirms that the given criterion was met.

Author(s)	Digital	Automatic		Frame rate (>1000 fps)	Saturated particle cloud			Sampling range	3D
		I	II		Scale	Supply	Wind speed		
Zhang et al. (2014)	*			*			*		
Ho et al. (2014)	*	*	*	*	*	*	*	*	
Gordon and McKenna Neuman (2011)	*	*			*	*	*		
Yang et al. (2009)	*			*					*
Creyseels et al. (2009)	*	*	*	*	*	*	*	*	
Gordon and McKenna Neuman (2009)	*	*				*	*	*	
Wang et al. (2009)	*	*	*	*		*			
Zhang et al. (2008)							*		
Noguchi et al. (2008)	*						*		
Wang et al. (2008)	*	*		*		*			
Zhang et al. (2007)	*			*			*		
Beladjine et al. (2007)	*			*			*		
Rice and McEwan (2001)				*		*	*	*	
Nishimurai and Hunt (2000)						*	*		
Rice et al. (1996)				*		*	*	*	
Rice et al. (1995)				*		*	*	*	
Nalpanis et al. (1993)				*		*	*		
Willetts and Rice (1986)				*		*	*	*	
White and Shulz (1977)				*		*	*		

the size and arrangement of particles within the bed surface create a substantial amount of randomness within trajectories comprising the saltation cloud. If the concentration of mass is high, particle to particle collisions can even occur during flight. In practice, particle trajectory velocities and angles are modeled by probability density functions, often having either a normal or lognormal form. Entrainment initially occurs through fluid drag, but with the consequent acceleration that occurs during flight, saltating particles eventually attain sufficient energy to either rebound and/or splash others out of the surface upon impact. Splash has been studied in a number of empirical investigations, although less commonly for steady state or saturated conditions (Table 1), beginning with the early, high-speed photography techniques of Rice et al. (1995). These workers confirm that the impact angle (α_2) of saltating particles is remarkably constant between 10° and 15°, with the largest angles generally being associated with coarse textured sediments. Angles of rebound (20° coarse $< \bar{\alpha}_1 <$ 40° fine), and particularly those for particle splash (40° coarse $< \bar{\alpha}_1 <$ 60° fine), are believed to be greater. While rebounding particles may retain as much as 50% of their momentum on average, the velocities of splashed particles are generally about an order of magnitude lower than that for the impacting particle. The number of splashed particles varies from 2 to 6 for a given impact, depending upon the relative particle diameters/mass. Few comparable measurements exist for steady state conditions involving a boundary-layer that is saturated with particles, and unfortunately, none for trajectory angles which depart from the time-averaged direction of the streamwise air flow.

3. Methods

3.1. Wind tunnel experiments and data collection

Thirty-nine experiments involving the measurement of particle trajectories during saltation were carried out in the Trent University Environmental Wind Tunnel (TEWT). The facility is a low speed, boundary-layer simulation tunnel with an open loop, suction design. It has a working section length of 13.5 m with a cross section that is 77 cm high by 70 cm wide, all of which is contained in a large environmental chamber with precise temperature (±0.5 °C) and humidity control (±2%). The air entering the intake at the tunnel entrance is first straightened as it is drawn through a honeycomb straw filter, then is compressed and accelerated through a 2D bell, and finally, is tripped as it passes over an array of 2 cm high doweling to initiate a shearing flow. The wind speed in the freestream (U_∞) is monitored by three pitot tube anemometers mounted along the center axis of the test section, and is regulated to within 1% by the rpm of the fan unit via AC variable control of the motor. Further details concerning the tunnel facility can be accessed at http://people.trentu.ca/~cmckneuman/website/facilities.html, and are provided in early papers by McKenna Neuman et al. (1996) and Nickling and McKenna Neuman (1997).

In order to study a saltation cloud in steady state, the entire bed of the tunnel was filled with well-sorted coarse quartz sand (median particle diameter, d = 550 μm), and then leveled to a depth of 2 cm. With U_∞ set to 8 ms^{-1} giving a friction velocity (u^*) of ~0.38 ms^{-1}, the boundary-layer flow was seeded with similar particles trickled into the working section from a hopper positioned 0.5 m downwind of the inlet. This served to initiate the development of saltation within the upwind sections of the tunnel, and thereby, extend the length of the test bed over which the flow was saturated with particles. In comparison, the wind speed threshold for fluid entrainment of the particles considered in this study is 6.5 ms^{-1} or u_t^* = 0.30 ms^{-1}, giving u^*/u_t^* = 1.3. At the downwind location of the PTV equipment at 10.5 m, the bed elevation was unchanged throughout the experiment, which confirms that the flux divergence was zero. Indeed, detailed profiling of the mass transport rate, the fluid momentum flux, and the turbulence intensity along the entire streamwise axis of the TEWT facility in earlier experiments by North (2014) suggests that the aeolian transport system reaches steady state approximately 4 m from the upwind edge of a bed of medium sand (d = 250 μm), with no evidence of an overshoot. This distance is identical to that measured in the field by Elbelrhiti et al. (2005) for sand having a mean particle diameter of 185 μm, in comparison to 1.75 m reported by Andreotti et al. (2010) for a wind tunnel experiment involving fine sand (d = 120 μm) for which u^*/u^*t = 1.5. During the present experiments, the tunnel was stopped after each period of particle trajectory measurement and the entire sand bed thoroughly re-mixed to minimize the development of particle-scale armouring over time. The bed surface was then re-leveled in preparation for the subsequent run. Given the constraints imposed by data storage capacity and processing time, the effects of a varied U_∞ were not addressed in this particular study.

The Particle Tracking Velocimetry (PTV) system operated at the TEWT facility (Fig. 1) consists of a 1 Watt, 532 nm, Nd-Yag laser and a pco.dimax HD™ high speed camera that captures grayscale images of illuminated sand particles passing through a 1.5 mm thick light sheet that intersected the bed surface over a distance of ~120 mm. In order to measure particle trajectories aligned at an angle (θ) to the mean airflow along the centerline of the wind tunnel, the light sheet orientation was adjusted from 0° to 60° in 5° increments. The camera was also repositioned each time to maintain a perpendicular line of sight. Three replicate experiments were carried out for each of 13 angles. Given an image resolution of 1920 × 720 px, a frame rate of 1500 fps, and an exposure time of 200 μs (required to minimize particle image distortion or streaking), 48 gigabytes of data were collected every 4.0 s, the equivalent sampling period for each experiment as limited by the camera memory. Further details concerning image processing, trajectory identification and the analysis of particle dynamics are reviewed in the following section.

3.2. Image processing and particle trajectory identification

Within the context of this paper, a trajectory is defined as a collection of images that represent some proportion of the path of a given particle moving within the boundary-layer flow. Apart from a small number of exceptions, the entire ballistic motion from ejection to impact generally is not captured in the photographic record. Compiling particle trajectories from the PTV camera frames requires extensive post processing. Two Matlab™ programs were written for this purpose. The first program processes the raw data by reducing noise, detecting the surface of the test bed, and identifying any particle images within the point cloud. The second program then uses these images to isolate, compile, and analyze discrete particle trajectories.

Frames downloaded from the high speed camera contain particle images that are superimposed upon a substantial amount of background 'noise' within the 100 mm × 35 mm viewing area. This noise was reduced by first subtracting the average frame brightness value from each pixel. The image then was converted to black and white using the 25th percentile of brightness as the threshold. This process further ensured that only particles passing through the focal plane of the camera were included in trajectory detection. The bed surface was detected using a custom edge finding algorithm applied to the bottom of each image. Finally, the particle images were isolated using a built-in image toolbox function, *imfindcircles()*, that detected all circles and provided the center coordinates and radius for each. The sensitivity and edge threshold values required by this function were calibrated manually for the experiments reported in this paper. Comparison of the particle size

distribution obtained by sieving with an analysis of optical data obtained from the camera (Fig. 2) confirms that the TEWT PTV system successfully captures the entire range of particle diameters present in the given test material. Flaring of the light scattered from the facets of quartz particles can enhance their appearance in high speed photography, which is an asset for detection of the finest particles, but also can lead to exaggeration of the coarse tail of the distribution as shown in the figure. This problem will be revisited in Section 4.3.

In order to link particle images (now represented as circles) across multiple frames into a single identifiable trajectory, the Expected Particle Area Search (EPAS) method was developed specifically for the purposes of the present study. As illustrated in Fig. 3, the search begins with a single particle image ($i = 1$) found in a given frame (F_0). Inputs for the EPAS method include Initial Search Radius (ISR), Secondary Search Radius (SSR), and the particle radius comparison ratio (RCR). If a particle from the next camera frame (F_{0+1}) is found to be within the chosen ISR (110 pixels) of the center of i_1 and of similar radius (RCR of 75%), then it is suspected to lie within a trajectory. Extrapolation of the vector between this initial particle pair is used to predict an expected location for the associated particle image in the third frame (F_{0+2}). If indeed a third particle image is found that is within the selected SSR (e.g. 12 pixels) of the expected particle area (EPA), and it is also of similar radius (again using an RCR of 75%), then all three images are assumed to represent the same sand particle. However, if no particle image is detected within the expected search area, then the initial pairing is rejected and the program selects a new particle image from F_0 and continues its search. Once a trajectory has been confirmed, the EPAS program continues to identify additional particle images along the given path line until no further instances are detected (Fig. 3). For a particle moving in a straight line at constant velocity, the EPAS method essentially compiles the trajectory from a sequence of vectors of fixed length and orientation, so that the mean particle velocity (U) and trajectory angle is the same as that for each segment. In the specific case of a particle that is accelerated through fluid drag, for example, the search radius for the particle image allows for a small amount of adjustment in the vector length and orientation throughout the time series. Once a given trajectory has been identified and extracted, the associated particle images are omitted from subsequent EPAS searches. With increasing from 3 to 5 the minimum number of particle images constituting a trajectory (MTL), the probability of an incorrect identification was found to drop below 0.001 (Fig. 4a).

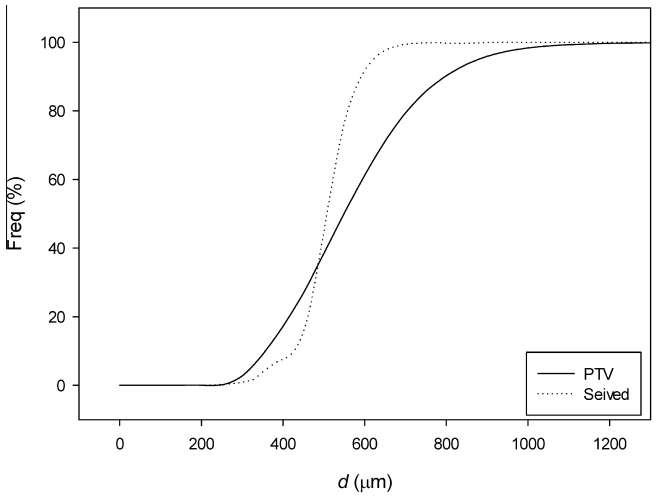

Fig. 2. Particle size distribution for sieved particles as compared to that derived from particle images captured on camera.

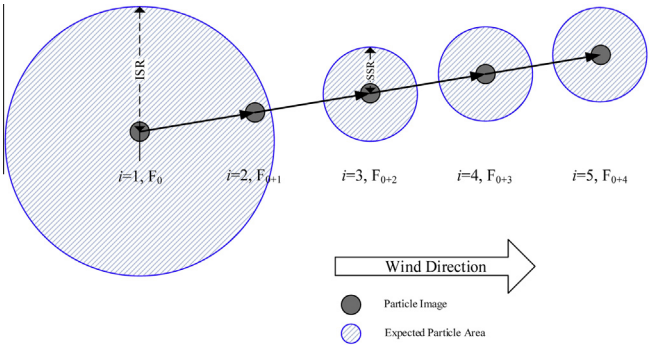

Fig. 3. Schematic illustrating the Expected Particle Area Search (EPAS) procedure for a five particle trajectory. ISR = Initial Search Radius, SSR = Secondary Search Radius, EPA = Expected Particle Area.

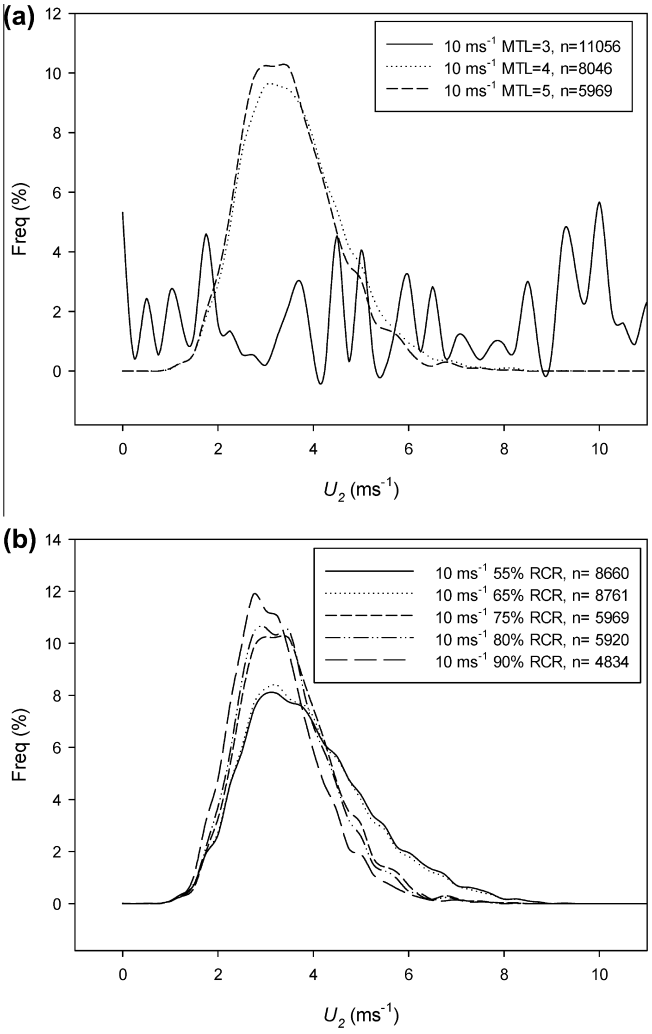

Fig. 4. Frequency distributions of the horizontal velocity of incoming particle trajectories detected by PTV using MTL of 3, 4 and 5 (a) and Radius Comparison Ratios (RCR) of 0.55, 0.65, 0.75, 0.80 and 0.9 (b). For this initial calibration exercise, $U_\infty = 10\ \mathrm{ms}^{-1}$ and the images were processed with ISR and SSR values of 110 and 12 pixels respectively.

Fig. 5 provides examples of particle trajectories detected in five separate experiments: three at $\theta = 0°$ (a, b and c), and one at each of 25° (d) and 50° (e). The flight path varies from long parabolic trajectories to linear segments containing just a few particle images.

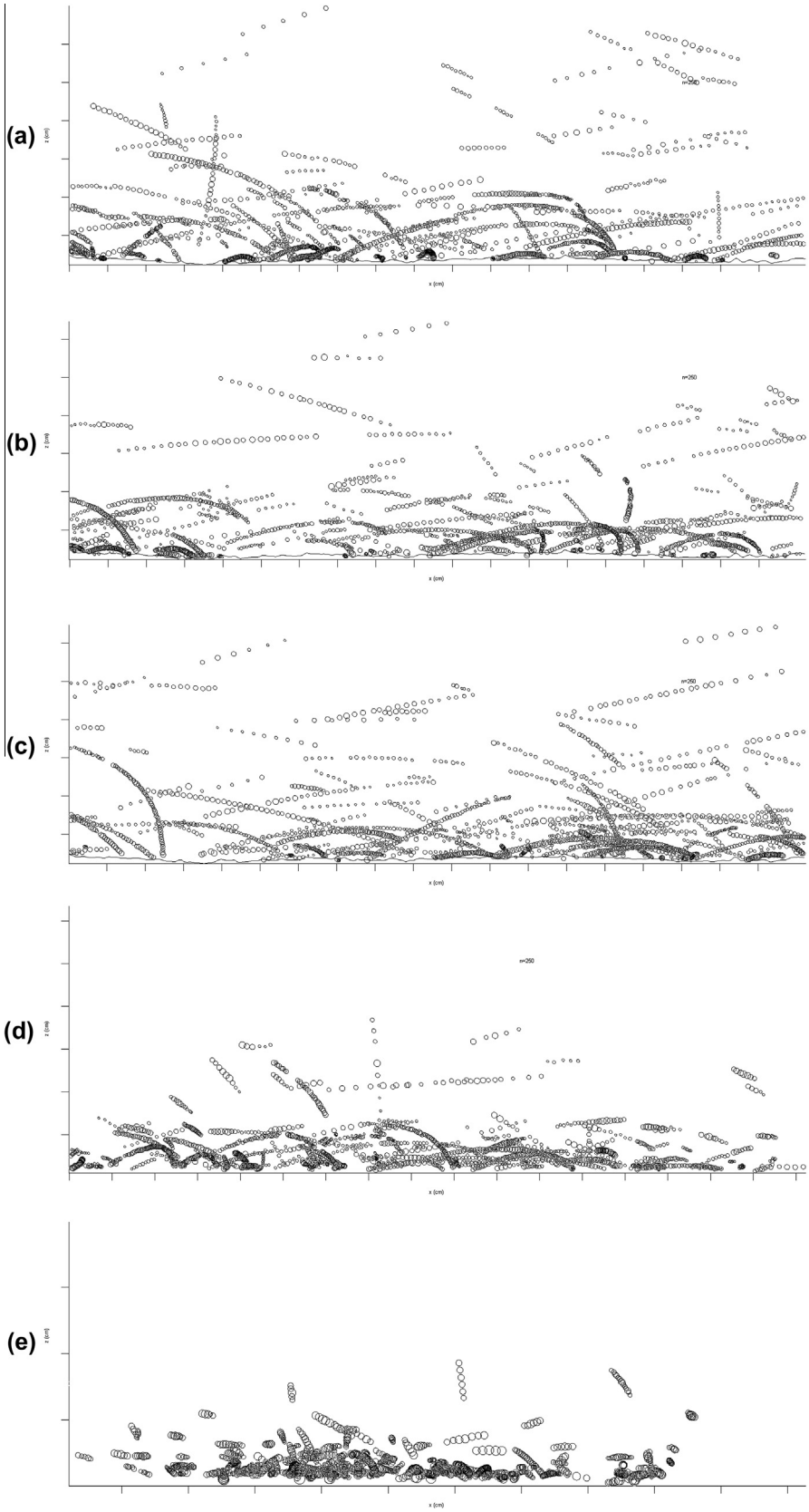

Fig. 5. Samples of particle flight paths identified using the EPAS method. The particle position at each time step (1/1500th s) is displayed as a circle, with a radius matching that of the original particle image at the respective *x,y* centroid. Plots (a–c) show trajectory segments sampled within a plane aligned with the mean air flow direction, as compared to plots (d) at a spanwise angle of 25° and (e) at 50°. In each case, the length scale between tick marks is 5 mm.

Indeed, Fig. 6 shows that about 1/5th of all 2×10^5 trajectory segments detected were short ($n_j = 5$, as constrained by the MTL), while those containing more than 15 particle images were relatively uncommon. Complete trajectories, in which particles departed from and then returned to the bed surface, were rarely sampled (<1/1000). In a small number of instances, a given trajectory is subdivided into several segments as a result of the rejection of intervening particle images that were either unacceptably small or absent owing to poor illumination. This introduces a minor exaggeration of the number of particles sampled. A noteworthy distinction is evident between the linear segments of fast moving saltators moving at heights of 10 mm or more, and the dense curtain of low energy particles hopping along very near the bed surface ($z \leqslant 3$ mm). In the few instances where the full length of the ballistic trajectory is captured, the acceleration of the particle by the fluid drag of the wind is quite remarkable and largely occurs in a forward direction near the top of the particle's path over a relatively narrow range in elevation ($5 < z < 10$ mm).

3.3. EPAS calibration

Due to the high sensitivity of the EPAS method to the required values for the input parameters, it must be carefully calibrated for the specific experimental conditions. As suggested in Fig. 3, the Initial Search Radius (ISR) must be large enough to encompass the entire distribution of particle speeds, while the Secondary Search Radius (SSR) must be sufficient to accommodate particle acceleration (or deceleration) throughout a given trajectory. However, if both parameter values are excessively large, the processing time and the probability of erroneous trajectory detection increase. Similarly, the Radius Comparison Ratio (RCR) must not only be large enough to reject erroneous particle image associations, but also small enough to account for a change in the apparent radius of a particle as it spins and exposes varied surface facets to the field of view of the camera. An ISR of 110, with the given image size and scale, allows for the detection of all particle velocities under 14 ms^{-1} and a SSR of 10% of the ISR accommodates a reasonable amount of acceleration.

After optimizing the values of ISR, and SSR, and choosing a conservative RCR value of 90% for trajectories based on a minimum of 3 particle images, it was discovered that ~5% of the trajectories identified by EPAS were invalid when verified by manual methods involving complex pattern recognition using the human mind. For this reason, the program was revised to define a minimum trajectory length (MTL) as having 5 particles. When these new results were manually verified, no invalid trajectories (e.g. involving overlapping flight paths, inter-particle collisions, and noise incorrectly identified as a particle image) were found in more than 1000 samples. In addition to manual verification, the distributions of horizontal velocity were evaluated for saltation trajectories containing varied numbers of particle images (n_j). As illustrated in Fig. 4a, MTL = 3 appears to be unacceptable, while good agreement is obtained between the distributions based on MTL = 4 and MTL = 5.

Lastly, it was necessary for the purposes of this study to isolate and analyze only those particles which had trajectories that were fully aligned with the plane of the light sheet (i.e. they did not enter and leave the sheet within the field of view). To ensure this, the RCR was calibrated for the unique lighting conditions of each experiment, given the following considerations:

(1) As a particle moves in and out of the illuminated field at a slight span wise angle, the Gaussian property of the light intensity causes the particle to appear larger in the PTV images as it gets brighter toward the center and smaller as it darkens toward to periphery. In order to detect trajectories that have a minimal span wise velocity component, the RCR must be set relatively high.
(2) The rotation of a faceted particle can cause its image to appear either brighter or darker in sequential camera frames, and therefore, the RCR must be low enough that the detection algorithm does not omit trajectories with high rotational speeds.
(3) The RCR must be large enough that the particle images being matched into trajectories are in fact the same particle.

Considerable effort was expended in determining suitable RCR values for the experiments reported in this paper, through both direct visual examination of sequential frames and comparison of the varied particle velocity distributions (Fig. 4b). Our findings suggest that an RCR > 75% is acceptably high without sacrificing the trajectory count. In addressing the effect of the Gaussian distribution of the laser, the light sheet was focused into a very thin sheet (1.5 mm) so as to attain relatively consistent illumination of the particles.

Appendix A provides further validation of particle velocities obtained using the PTV-EPAS method through comparison with independent LDA measurements.

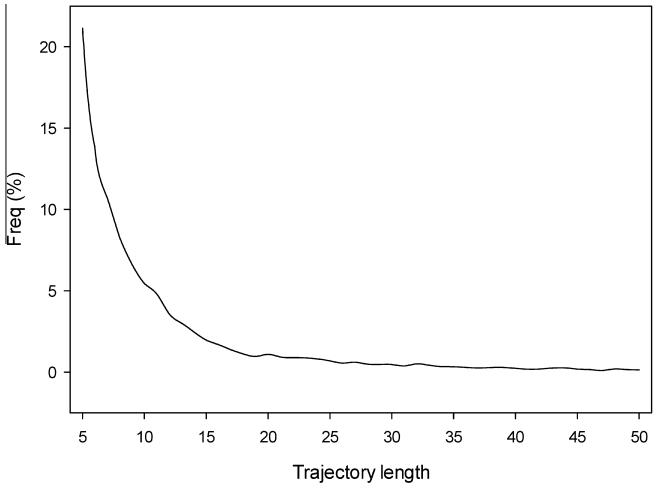

Fig. 6. Frequency distribution for n_j, the number of particle images represented in a given trajectory segment. The minimum for n_j was preset to 5.

4. Results and discussion

4.1. Distributions of particle count and component velocity

To this date, no detailed measurements have been carried out concerning the proportion of grains within the saltation cloud moving in trajectories that are not aligned with the mean wind, and thus, have a significant spanwise displacement at their point of impact. As shown in Fig. 7, the data obtained in the present set of wind tunnel experiments suggest that only 12% of all trajectories sampled were aligned with the mean air flow along the centerline of the wind tunnel working section ($\theta = 0°, \pm 1°$). Up to 95% were contained within $\theta \leqslant 45°$, although a small number of splashed grains were observed moving within the light sheet at very high angles around 60°. The frequency of occurrence of particle flight along a plane of varied alignment with the mean air flow (Fig. 7) can be described in cumulative form by the following 3-parameter sigmoidal relation,

$$F = \frac{a}{1 + e^{-\left(\frac{\theta+\theta_0}{b}\right)}} \quad (1)$$

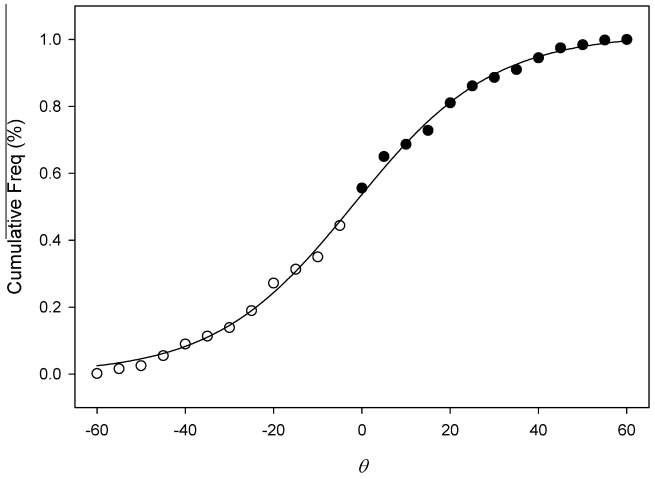

Fig. 7. Cumulative frequency of the number of observed particles moving in trajectories aligned at varying spanwise angles (up to 60°) from the mean flow direction defined as $\theta = 0°$. The solid circles represent the direct measurements obtained in this study; that is, particles veering to the right when viewed from a fixed point above the bed surface. The open circles represent an extrapolation for particles veering to the left and are intended to convey particle diffusion throughout the full particle cloud, assuming that it is symmetrical. The sigmoidal curve shown is a least squares fit to the data set with $r^2 = 0.99$.

where $a = 1.0$, $b = 15.8$, and $\theta_o = 1.8$. It is assumed herein that the distribution of particles contained within the saltation cloud was symmetrical about the longitudinal axis of the tunnel, given that it was only feasible to measure positive values for θ since the back wall is inaccessible. Unfortunately, it is not possible to obtain a reliable measure of the particle concentration from the images obtained, owing to the rejection of a considerable number of potential trajectories that do not meet the stringent criteria established for the EPAS method, as well as the omission of all particles that were not precisely aligned with the light plane.

Apart from the number of particles entrained into the airflow, the velocity components of these particles in each of the three dimensions (u_x – streamwise, u_y – spanwise, u_z – vertical) is of particular interest to saltation modelers who need to parameterize emerging 2.5D and 3D saltation models (Kang, 2012; Kok, 2010; Kang and Zou, 2014). For the present study, the mean particle velocity (U) was calculated for any given trajectory by averaging the distance between the centroids for each successive pair of particle images and then dividing this value by the time step between camera frames. Particle acceleration was not quantified, but is presently under consideration in regard to an extension of this work. The horizontal velocity U_h obtained for the flight path of each particle within the illuminated slice of the saltation cloud was further used to determine the component u_x from $U_h \cos\theta$, and u_y from $U_h \sin\theta$. Figs. 8a–c provide frequency distributions for all three velocity components based on approximately 2×10^5 particles. These distributions are further classified by whether the particles were ascending or descending at the time of sampling. In all cases, they are approximately lognormal. The absolute magnitude of the mode for each velocity distribution changes with the component, but is not determined by the vertical orientation of the trajectory segment. With regard to the streamwise component (u_x), the mode of the distribution sits around 0.2 ms^{-1}, and is higher than the values for the spanwise and vertical components, which are identical at 0.05 ms^{-1}. Similarly, there is a slightly higher proportion of particles travelling at faster speeds ($\sim$1 ms^{-1}) in the right tail of the u_x distribution for the descending grains, which is likely a result of being accelerated by wind drag during their flight, as compared to those ejected from the bed surface. As expected, this effect is not apparent for the vertical and spanwise components. While

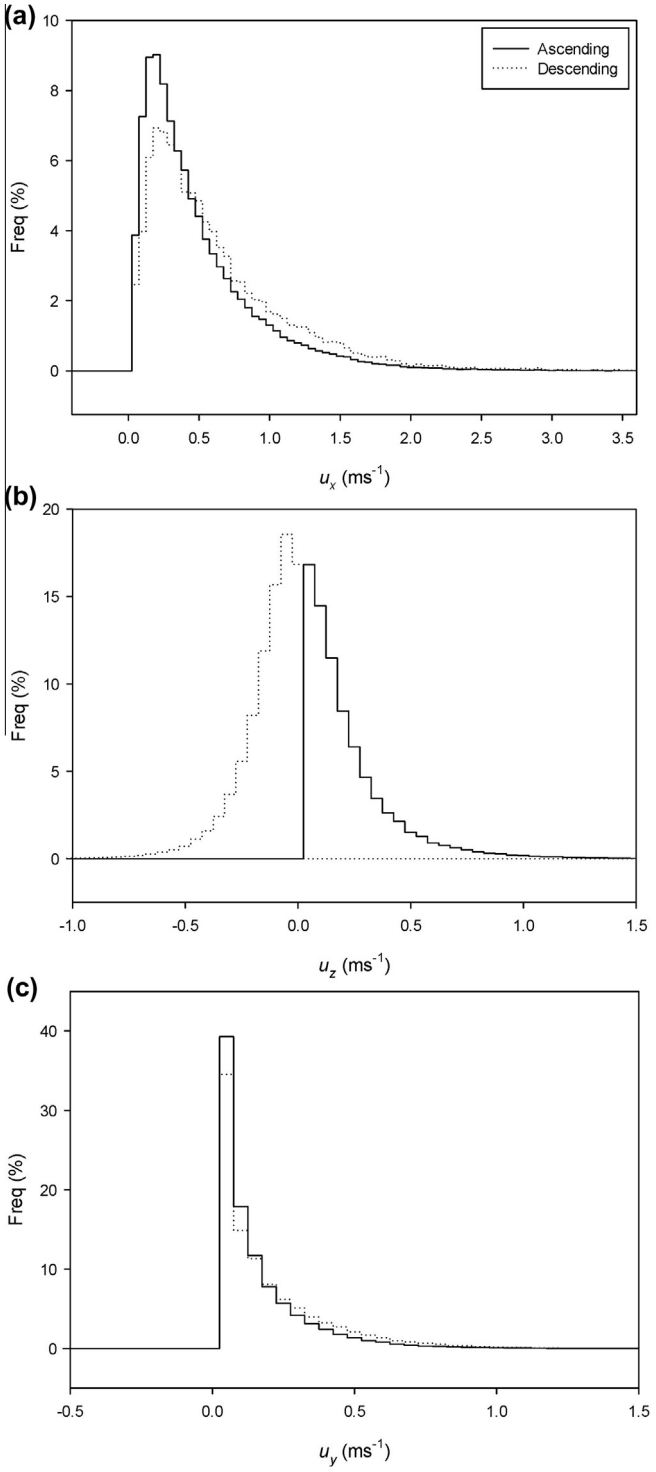

Fig. 8. Frequency distributions for the particle component velocities, u_x, u_z, and u_y, as determined from the entire set of particle trajectories sampled.

several particles did reach high speeds, they represent such a small proportion of the total population that they are not visible in these frequency plots.

4.2. Effect of the spanwise angle on particle trajectory characteristics

Bagnold's earliest descriptions of saltation suggest that the entrained sand particles follow ballistic trajectories, and as such, are accelerated by wind drag during their flight prior to impacting

the bed surface at a low, near constant angle (Bagnold, 1941). Anderson (1987), on the other hand, later refined this description of the saltation cloud to recognize the presence of relatively large, low energy particles that travel in very small hops very near the bed surface, often initiated as splash, and do not attain sufficient momentum to rebound. He described this transport process as reptation. The distinction between the two modes of transport is not well quantified, however, with regard to the particle velocity components, trajectory scale and shape, and the proportionate contribution to the total mass transport rate. Indeed, the small number of published measurements (Table 1) largely pertain to wind aligned particles transported in an unsaturated saltation cloud. In comparison, the present study examines particle motion on a very fine scale down to 1 particle diameter above the bed surface, and over a wide range of spanwise angles in a fully adjusted (saturated) transport system.

Fig. 9 compares the cumulative frequency distributions for U and α, with each curve representing a 10° increment in the spanwise angle of the flight path. Ascending particles are shown in the column on the left (plots a and c), as compared to descending particle flight paths on the right (plots b and d). When the full population ($N = 2454$) for replicate one is filtered to consider only portions of trajectories within 3 particle diameters of the bed surface, representing impact and ejection phenomena only, the frequency distribution for U ($N = 1950$) is approximately identical to that for all trajectories detected regardless of length and distance from the bed surface. The same is true for the distributions of the filtered particle trajectory angle, as compared to those for all ascending and descending segments. In order to reduce excessive clutter, only the data for the first of three experimental replicates are included in Fig. 9.

The distributions shown are positively skewed, although the amount of asymmetry is most extreme for the trajectory angle (α) as compared to the particle speed. Only 3% of all trajectories sampled involved particles moving slightly upwind while rising from the bed surface, and they are not included in Figs. 9c and d. With an increase in the departure of the trajectory from the wind aligned plane, the distribution of U shifts to the left, opposite to that for α. The range in particle speed spans almost two orders of magnitude, from extremely slow moving particles to several saltators moving at $\sim 4\ ms^{-1}$, about half the speed of the freestream flow in the core of the wind tunnel.

Clear evidence of a systematic trend emerges in plots (Fig. 10) of the median values (U_{50} and α_{50}) derived for all three sets of experiments. Despite the stochastic nature of the transport process and the bed surface composition, the agreement among these replicates is very good for any given spanwise angle. As a general rule, the median particle velocity appears to drop linearly by

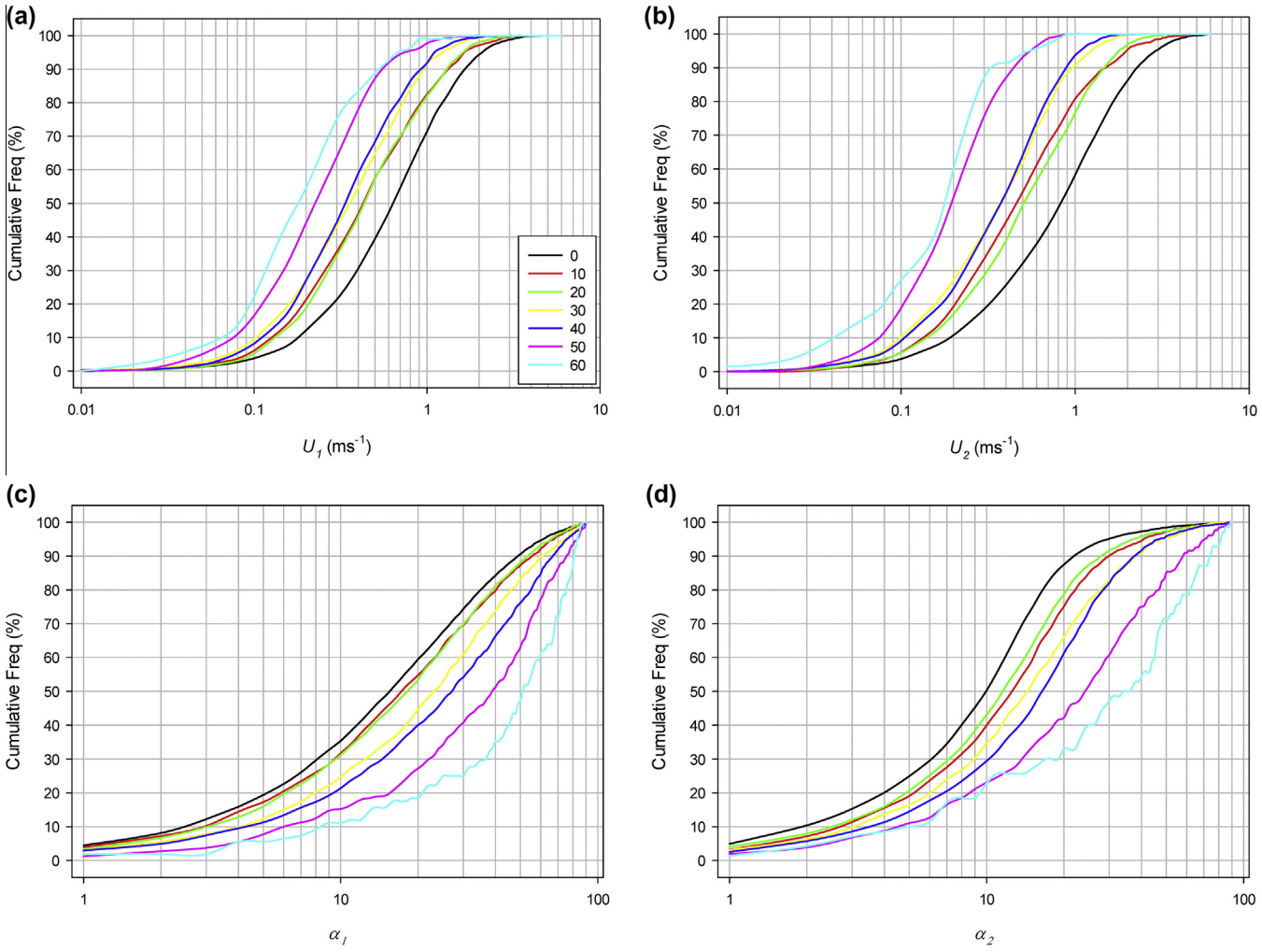

Fig. 9. Cumulative frequency distributions of U and α over a range of values for the spanwise angle θ (in 10° increments). Plots (a) and (c) in the left column refer to ascending particles, and in the right column, (b) and (c) to descending particles.

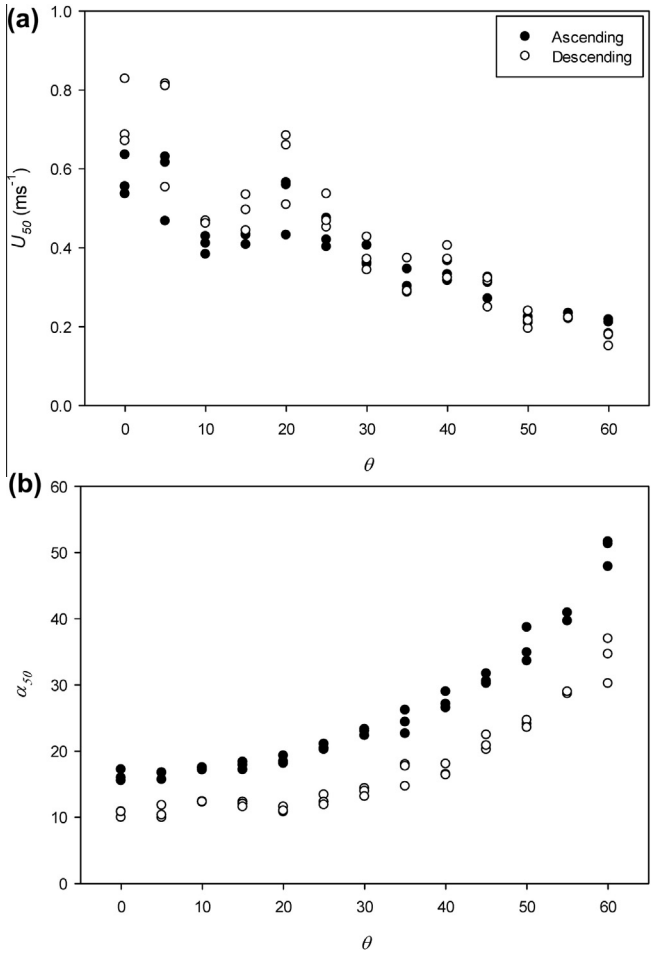

Fig. 10. The influence of θ on U_{50} and α_{50}, the medians of the associated distributions of the mean particle speed and particle trajectory angle, respectively. Solid circles represent ascending trajectory segments, and open circles the subpopulation of descending particles. In any given plot, each of three experimental replications is provided its own point symbol.

$\sim$0.03 ms^{-1} for every 5° increase in the spanwise angle. For spanwise angles under 25°, particle acceleration via fluid drag is evident with $U_{2,50}$ often exceeding $U_{1,50}$ (Fig. 10a). At higher spanwise angles, however, there is little distinction in the median particle velocity with reference to either the experimental replicate or the inclination of the trajectory segment. In comparison, α_{50} is relatively insensitive to variation in $\theta \leqslant 20°$, but rises substantially with further increases in the angle of departure from the mean air flow direction up to 60° (Fig. 10b). The angle of descent for particles closely aligned with the airflow averages around 10–12°, which is in good agreement with published values (e.g. Bagnold, 1941; Rice et al., 1995; Shao, 2010). The median angle associated with the ascending segments of all particle trajectories sampled is consistently higher, by $\sim$5–12°. On the whole, the results from the present study appear to support the premise that as θ increases, an increasing proportion of the particle transport consists of small, low energy hops (reptation). Certainly, at $\theta \geqslant 45°$ reptators likely constitute the whole of the population of moving grains, though less than 5% of the 2×10^5 trajectories sampled.

In further confirmation of this statement, the mean diameters of the particle images sampled remain steady around 500–550 μm for spanwise angles between 0° and 35°, but beyond this displacement from the mean airflow, appear to become consistently larger. This trend is in agreement with other measurements that suggest a change in the dominant transport mode.

4.3. Particle-borne kinetic energy

A majority of numerical models of saltation assume that all particle motion is wind aligned, with the transfer of momentum from the fluid to the particle cloud providing the mechanism for attaining steady state transport. The present findings are important in that they not only suggest that just 1/8th of all particle trajectories are precisely wind aligned, but also, the work needed to accelerate each particle from rest to its sampled velocity is systematically altered as θ increases. The same amount of work is required to decelerate the particle to a state of rest upon impacting the surface and can be calculated from the particle's kinetic energy.

The large proportion of low speed trajectories sampled within the cloud of sand in this study arises from measuring: (i) within a fully adjusted boundary-layer flow that was saturated with particles, (ii) at and very near the bed surface within the densest region of the sand cloud, and (iii) within planes having a varied and substantial spanwise component. Although high speed trajectories were indeed observed well above the bed surface, they were relatively few in number. As a result it is plausible that 2D models of saltation parameterized by early PTV measurements (Table 1) may underestimate the amount of particle splash and related energy expenditure within the transport system, while overestimating velocities associated with particle saltation. Further consideration is given below to the apportioning of kinetic energy within the sand cloud.

One of the advantages of the PTV-EPAS tool is the capability to derive an estimate of the kinetic energy (E) of a given particle that accounts for the orientation of its trajectory (E_x, E_y, or E_z), as for example:

$$E_{x,j,k} = \frac{1}{2} m_{j,k} * u_{x,j,k}^2 \tag{2}$$

where $u_{x,j,k}$ is the particle velocity component in the streamwise direction (x) for the jth trajectory within the kth θ plane. The total kinetic energy of the particle is then the sum of all three components,

$$E_{j,k} = E_{x,j,k} + E_{y,j,k} + E_{z,j,k} \tag{3}$$

with

$$E_k = \sum_{j=1}^{n_k} E_{j,k} \tag{4}$$

representing the net kinetic energy of all n_k particles sampled within the kth spanwise plane.

The fine resolution of the high speed camera allows for particle image radius measurements that can be used in calculating a first approximation the particle mass (m_j) associated with the jth trajectory. In the context of the present experiments, m_j is calculated from Eq. (5) below by assuming that each particle sampled had a spherical shape and constant density (ρ = 2650 kg m^{-3}),

$$m_j = \rho \frac{4}{3} \pi \left(\frac{\sum_{i=1}^{n_j} r_{i,j}}{n_j} \right)^3 \tag{5}$$

where the particle radius (r) is essentially taken to be the average obtained from n_j image measurements within the jth trajectory. While some degree of error is unavoidable in measuring particle size via optical methods, particle mass is shown below to have very little influence on the relative proportion of energy distributed through θ for the well sorted sand used in the present experiments.

The partitioning of the total kinetic energy (KE) sampled within the sand cloud among each of the illuminated planes (E_k/KE) is summarized in Fig. 11. Within this figure, the particle energy is further segregated into subpopulations of ascending ($N = 9.0 \times 10^4$)

and descending ($N = 8.7 \times 10^4$) particles. The observation that these subpopulations vary in number by only 3% when integrated over all angles lends further support to the earlier statement that the transport system under investigation had reached steady state. It is also important to clarify for this figure that only measured data are displayed; that is, the data are not mirrored as in Fig. 7. It appears that as little as 1/8th of the total kinetic energy sampled within the sand cloud is partitioned into particle trajectories that are strictly aligned in the streamwise direction ($\theta = 0°$). With increasing θ, E_k/KE decreases in close proportion to a similar decline in the relative number (n_k/N) of particle trajectory segments sampled within each subpopulation, regardless of the direction of vertical motion (up vs down). In effect, despite the systematic changes observed in particle velocity (Figs. 9 and 10) and transport mode with flight direction, variation in the kinetic energy borne by the sand particles is primarily determined by their number. The general decay with θ shown in Fig. 11 is subject to several perturbations (e.g. at 10° and 15°) which could have resulted either from instantaneous variations in the spatio-temporal organization of the saltation cloud (i.e. streamers) or from grain-scale packing/armouring within the bed surface. A greater number of experimental replications would likely smooth the trend, but also increase the data storage demands and processing time beyond what is currently feasible within the facility. The proportion of particle energy directed vertically relative to the horizontal component within a given viewing plane ($E_{z1,k}/E_{x,k}$ and $E_{z2,k}/E_{x,k}$) shows little variation over a range of spanwise angles not exceeding 35°, but beyond this continually increases with θ, particularly in the case of the ascending particles or $E_{z1,k}$. This outcome is consistent with the suggestion that where there is a strong spanwise component in the near-bed motion, the effects of fluid drag are substantially reduced and the transport mode is dominated by splash.

4.4. Limitations and future developments

While this study confirms that a given particle is likely to be ejected at a spanwise angle that is different from that for the particle trajectory initiating its motion through impact, it is impossible at present to monitor particle motion in 3D space within a large volume of the boundary layer flow. As a consequence, EPAS-PTV data cannot be used to link the characteristics of the ejecta to a specific collision, unless all particle trajectories involved in a given collision remain with the thin light sheet. The main point of this paper, of course, is that they don't.

The scattering of light within the thin sheet illuminating the sand particles results in a reduction in brightness as the concentration of particles increases toward the bed surface. Where the mass concentration is relatively low (i.e. within the outer fringe of the saltation cloud several cm above the active bed), sampling remains possible over a wide range of wind speeds. When the wind speed is high, however, inadequate illumination presents a challenge in obtaining measurements directly at the bed surface. For this reason, the calibration experiments described in this study were carried out over a range of wind speeds up to 13 ms^{-1} at an elevation of 0.03 m, as compared to the measurements of particle dynamics obtained at or very near the surface for which U_∞ was lowered to 8 ms^{-1}. Advancements in camera and laser technologies, as well as noise filtering tools, have provided improvements in this regard but they are not without limits. While more powerful lasers can provide additional illumination, problems of flaring increase, especially that for the bed surface. PTV involves a large number of tradeoffs, but even when operating a fully optimized system, highly energetic mass transport events remain difficult to measure at the particle scale.

Work is ongoing to calibrate the PTV system to adjust for an exaggeration of particle size in the coarse tail of the distribution (Fig. 2) that is associated with flaring when quartz particles are illuminated within a laser sheet. Some poorly focused particle images outside the narrow 1.5 mm depth of field of the camera may also appear larger and darker, while decreasing illumination toward the outer edge of the light sheet can make others appear relatively small. The rotation of oblate or faceted particles can also present problems for trajectory identification and evaluation of particle size. As outlined in Appendix A, however, highly inconsistent particle diameters are rejected by the EPAS trajectory identification algorithm.

Finally, the authors recognize that the analysis of the data obtained in this study remains at a fairly rudimentary stage. Further work examining particle acceleration and the grain-borne stress, as well as differentiation of the particle dynamics with

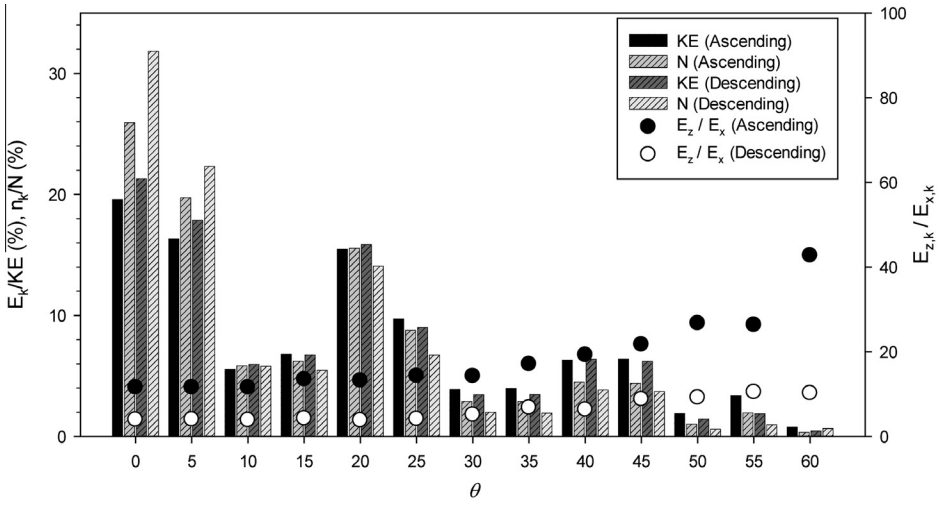

Fig. 11. Bar graph illustrating the partitioning of the total kinetic energy sampled within the particle cloud ($E_k/KE\%$) among each of the illuminated planes, designated by θ. The general trend toward decreasing kinetic energy with increasing spanwise angle appears to be primarily driven by a similar drop in the proportionate number of trajectories ($n_k/N\%$) sampled. The portion of the particle-borne kinetic energy directed vertically relative to the streamwise component ($E_{z,k}/E_{x,k}$) is overlain on the plot as point symbols. The legend distinguishes the trajectory segments sampled by their inclination (ascending versus descending).

distance from the bed surface, for example, is currently in progress. Collaboration with the community of aeolian modelers is invited to compliment and assist in extending the experimental developments reported in this study.

5. Conclusions

Experimental observation of particles within a fully saturated saltation cloud has historically been a challenging task because of inadequate lighting, difficulties with surface detection, and a high degree of error associated with particle detection and trajectory identification. In this paper the EPAS-PTV method, based upon particle radius comparison, is first optimized to reduce trajectory identification errors and then validated through comparison with measurements obtained using laser Doppler anemometry (LDA).

Application of this technology in a novel wind tunnel investigation of the spanwise component of trajectories within a saturated saltation cloud reveals that less than 1/8th of particles travel directly along the path of the mean air flow. However, 95% of the particles sampled are contained within $0° \leqslant \theta \leqslant 45°$. This study provides the first direct measurements of the x, y and z components of particle velocity and their respective probability distributions. The alignment of the flight path is found to systematically alter the total velocity of a given particle, as well as its launch/impact angle. The observed decline in the proportionate particle-borne kinetic energy with increasing spanwise angle, however, is found to be driven primarily by the waning particle counts and not speed. At high angles, the primary mode of transport appears to shift from saltation to reptation. Such observations may have important implications for the parameterization of emerging 3D saltation models, as well as for understanding the inception and growth of small-scale aeolian bedforms in the context of particle diffusion, both of which are beyond the scope of the present paper. An extension of this 2.5D study is presently underway to quantify particle acceleration for the full parabolic trajectories captured and to determine the variation in U and d with elevation above the bed surface.

Acknowledgements

Funding in support of this work was provided through grants to C. McKenna Neuman from the Natural Sciences and Engineering Research Council of Canada (Discovery Grant) and the Canada Foundation for Innovation (CFI) (Microenvironments Laboratories). Bailiang Li provided key support in obtaining the LDA data. Early discussions with Jasper Kok and Hezi Yizhaq provided the incentive to pursue much of the work described in this paper, and in particular, inspired our attempt to measure the spanwise components of saltation. The authors are grateful for the efforts of two anonymous reviewers that led to substantial improvements in the paper.

Appendix A

In order to validate the EPAS methodology, beyond manual checks of the particle trajectories detected, a separate series of PTV experiments was carried out in conjunction with independent particle velocity measurements obtained with a laser Doppler anemometer (LDA). LDA has been previously employed in empirical investigations of saltation (e.g. Rasmussen and Sorensen, 2008; Taniere et al., 1997), providing a suitable reference technology by which the performance of the PTV-EPAS technique can be evaluated. The experiments were performed under the same wind tunnel conditions as those described in Section 2.1, but with a few alterations. In order to sample a sufficient number of grains with the Dantec™ 2D LDA, high wind speeds (10, 11, 12 and 13 ms^{-1}) and a longer sample time (25 s) were used. The sample volume (0.04 mm^3) of the LDA was collocated 10 cm upwind of the field of view of the pco.Dimax HD™ camera. Both instruments were positioned to sample 30 mm above the bed, as this was the lowest elevation at which the high density of saltation did not cause an overload of the Burst Spectrum Analyzer (BSA)™ for the LDA. The BSA settings were customized to measure sand grains, matching those reported in Li and McKenna Neuman (2012).

The results of this validation experiment are summarized in Table 2. It is apparent that with identical sample times, the PTV was able to obtain, on average, 32 times as many sample measurements as the LDA. This is attributed to both the disparate sizes of their respective sample volumes, with that for the PTV being 40,000 times larger, as well as to the capacity of the PTV to sample multiple grains simultaneously. The differences between PTV and LDA median velocities for both ascending and descending particles are small, on average only 0.3 ms^{-1} with the LDA value tending to produce the higher of the two measurements. Fig. 12 provides a more detailed comparison between the frequency distributions obtained for all particle velocities (U) measured by each instrument in the context of a single experiment for which the free-stream wind velocity was set at 13 ms^{-1}. Only the descending particle trajectories are selected for consideration, given that this condition produced the largest sample size for the LDA. The high degree of overlap between the medians for the cumulative

Table 2
Comparison of particle velocity (U) measurements obtained using PTV versus LDA technologies. The data are first segregated by the freestream wind speed established for the experiment and then by the vertical component (ascending versus descending) of the particle speed. The statistical summary provides the number of particles sampled (n), the median horizontal particle velocity (U_{50}) and the standard deviation (σ).

	U_{50} (ms^{-1})		σ (ms^{-1})		n	
	PTV	LDA	PTV	LDA	PTV	LDA
10 ms^{-1} ↑	2.05	2.18	0.79	1.73	7970	249
10 ms^{-1} ↓	3.32	3.57	1.01	1.99	5969	330
11 ms^{-1} ↑	2.26	2.78	0.86	2.08	10,669	287
11 ms^{-1} ↓	3.46	3.29	1.12	2.35	7946	463
12 ms^{-1} ↑	2.23	2.65	0.98	2.24	51,616	313
12 ms^{-1} ↓	3.28	3.93	1.32	2.44	31,536	509
13 ms^{-1} ↑	2.45	3.20	1.00	1.94	54,888	390
13 ms^{-1} ↓	3.70	3.825	1.49	2.42	36,954	604

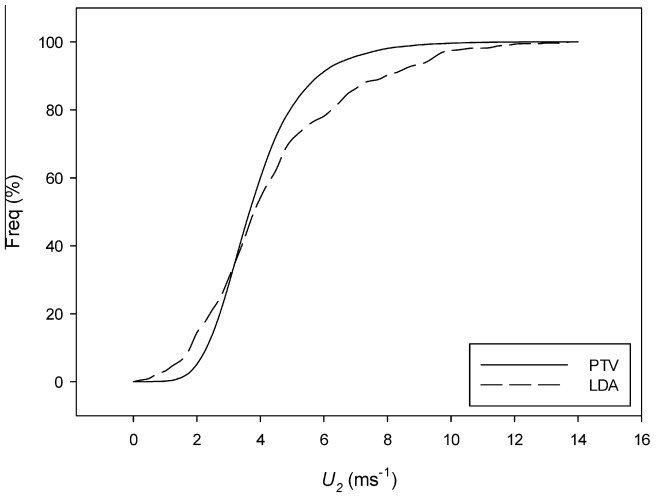

Fig. 12. Comparison of the distributions of U_2 derived from PTV and LDA measurements for experiments run at a freestream velocity of 13 ms^{-1}.

frequency curves demonstrates that in general, the particle velocity measurements obtained by the two instruments are in good agreement in this example. However, the standard deviation for the relatively small number of velocity measurements obtained with the LDA is roughly double that for the PTV and gives rise to more pronounced tails within the frequency distribution. With reference to the measurements reported in the main text, it is important to note that these particle velocities are substantially greater as they were obtained within the outer fringe of the saltation cloud at a free stream wind speed that was 5 ms^{-1} higher.

References

Anderson, R.S., 1987. A theoretical model for aeolian impact ripples. Sedimentology 34, 943–956.

Andreotti, B., Claudin, P., Pouliquen, O., 2010. Measurements of the aeolian sand transport saturation length. Geomorphology 123, 343–348.

Baas, A.C.W., Sherman, D.J., 2005. Formation and behavior of aeolian streamers. J. Geophys. Res. Earth Surf. 110 (F3), F03011.

Bagnold, R.A., 1941. The physics of Blown Sand and Desert Dunes. Methuen, New York.

Beladjine, D., Ammi, M., Oger, L., Valance, A., 2007. Collision process between an incident bead and a three dimensional granular packing. Phys. Rev. E 75 (6).

Creyseels, M., Dupont, P., Ould, A., Moctar, E., Valance, A., Cantat, I., Jenkins, J.T., Pasini, J.M., Rasmussen, K.R., 2009. Saltating particles in a turbulent boundary-layer: experiment and theory. J. Fluid Mech. 625, 47–74.

Duran, O., Claudin, P., Andreotti, B., 2011. On aeolian transport: grain-scale interactions, dynamical mechanisms and scaling laws. Aeolian Res. 3, 243–270.

Elbelrhiti, H., Claudin, P., Andreotti, B., 2005. Field evidence for surface-wave-induced instability of sand dunes. Nature 437, 720–723.

Gordon, M., McKenna Neuman, C., 2009. A comparison of collisions of saltating grains with loose and consolidated silt surfaces. J. Geophys. Res. 114.

Gordon, M., McKenna Neuman, C., 2011. A study of particle splash on developing ripple forms for two bed materials. J. Geomorphol. 129, 79–91.

Ho, T.D., Valance, A., Dupont, P., Ould, A., Moctar, E., 2014. Aeolian sand transport: length and height distributions of saltation trajectories. Aeolian Res. 12, 65–74.

Jackson, D.W.T., Beyers, J.H.M., Lynch, K., Cooper, J.A.G., Baas, A.C.W., Delgado-Fernandez, I., 2011. Investigation of three-dimensional wind flow behaviour over coastal dune morphology under offshore winds using computational fluid dynamics (CFD) and ultrasonic anemometry. Earth Surf. Proc. Land. 36 (8), 1113–1124.

Kang, L., 2012. Discrete particle model of Aeolian sand transport: comparison of 2D and 2.5D simulations. Geomorphology 139–140, 536–544.

Kang, L., Zou, X., 2014. Theoretical analysis of particle number density in steady aeolian saltation. Geomorphology 204, 542–552.

Kok, J., 2010. An improved parameterization of wind-blown sand flux on Mars that includes the effect of hysteresis. Geophys. Res. Lett. 37.

Kok, J.F., Parteli, E.J.R., Michaels, T.I., Bou Karam, D., 2012. The physics of wind-blown sand and dust. Rep. Prog. Phys. 75 (106901), 72.

Li, B., McKenna Neuman, C., 2012. Boundary-layer turbulence characteristics during aeolian saltation. Geophys. Res. Lett. 39.

Liu, X., Dong, Z., 2004. Experimental investigation of the concentration profile of a blowing sand cloud. Geomorphology 60, 371–381.

McKenna Neuman, C., Maxwell, C.D., Boulton, J.W., 1996. Wind transport of sand surface crusted with photoautotrophic microorganisms. Catena 27, 229–247.

Nalpanis, P., Hunt, J.C.R., Barrett, C.F., 1993. Saltating particles over flat beds. J. Fluid Mech. 251.

Nickling, W., McKenna Neuman, C., 1997. Wind tunnel evaluation of a wedge-shaped aeolian sediment trap. Geomorphology 18 (3–4), 333–345.

Nishimurai, K., Hunt, J.C.R., 2000. Saltation and incipient suspension above a flat particle bed below a turbulent boundary-layer. J. Fluid Mech. 417, 77–102.

Noguchi, K., Nezu, I., Sanjou, M., 2008. Turbulence structure and fluid-particle interaction in sediment-laden flows over developing sand dunes. Environ. Fluid Mech. 8, 569–578.

North, H., 2014. The effect of fetch on the development of the saltation carpet. Unpublished Honours thesis. Trent University.

Owen, P.R., 1964. Saltation of uniform grains in air. J. Fluid Mech. 20 (2), 225–242.

Rasmussen, M., Sorensen, M., 2008. Vertical variation of particle speed and flux density in aeolian saltation: measurement and modeling. J. Geophys. Res. 113.

Rice, M.A., McEwan, I.K., 2001. Crust strength: a wind tunnel study of the effect of impact by saltating particles on cohesive soil surfaces. Earth Surf. Proc. Land. 26, 721–733.

Rice, M.A., Willetts, B.B., McEwan, I.K., 1995. An experimental study of multiple grain-size ejecta produced by collisions of saltating grains with a flat bed. Sedimentology 42, 695–706.

Rice, M.A., Willetts, B.B., McEwan, I.K., 1996. Observations of collisions of saltating grains with a granular bed from high-speed cine-film. Sedimentology 43, 21–31.

Shao, Y., 2010. Physics and Modelling of Wind Erosion. Springer, Lexington, pp. 452.

Taniere, A., Oesterle, B., Monnier, J.C., 1997. On the behavior of solid particles in the horizontal boundary-layer with turbulence and saltation effects. Exp. Fluids 23, 463–471.

Valance, A., Rasmussen, K., Moctar, A., Dupont, P., 2015. The physics of Aeolian sand transport. C. R. Phys. 16, 105–117.

Wang, D., Wang, Y., Yang, B., Zhang, W., 2008. Statistical analysis of sand grain/bed collision process recorded by high-speed digital camera. Sedimentology 55, 461–470.

Wang, Y., Wang, D., Wang, L., Zhang, Y., 2009. Measurement of sand creep on a flat sand bed using a high-speed digital camera. Sedimentology 56, 1705–1712.

White, B., Shulz, J., 1977. Magnus effect in saltation. J. Fluid Mech. 81 (3), 497–512.

Willetts, B.B., Rice, M.A., 1986. Collisions in aeolian saltation. Acta Mech. 63 (1–4), 255–265.

Yang, B., Wang, Y., Zhang, Y., 2009. The 3-D spread of saltation sand over a flat bed surface in aeolian sand transport. Adv. Powder Technol. 20, 303–309.

Yang, J., Zhang, Y., Liu, D.Y., Wei, X.L., 2010. CFD-DEM simulation of three-dimensional aeolian sand movement. Sci. China Phys. Mech. Astron. 53 (7), 1306–1318.

Zhang, W., Kang, J., Lee, S., 2007. Tracking of saltating sand trajectories over a flat surface embedded in an atmospheric boundary-layer. Geomorphology 86, 320–331.

Zhang, W., Wang, Y., Lee, S., 2008. Simultaneous PIV and PTV measurements of wind and sand particle velocities. Exp. Fluids 45, 241–256.

Zhang, Y., Wang, Y., Jia, P., 2014. Measuring the kinetic parameters of saltating sand grains using a high-speed digital camera. Sci. China Phys. Mech. Astron. 57 (6), 1137–1143.